

Structure, force balance, and evolution of incompressible cross-tail current sheet thinning

M. H. Saito,¹ D. Fairfield,¹ G. Le,¹ L.-N. Hau,² V. Angelopoulos,³ J. P. McFadden,⁴ U. Auster,⁵ J. W. Bonnell,⁴ and D. Larson⁴

Received 14 March 2011; revised 18 July 2011; accepted 23 July 2011; published 19 October 2011.

[1] THEMIS five-point observations on April 8, 2009 were used to study thinning of the current sheet in the near-Earth tail that led to the onset of a small substorm. Taking advantage of a fortuitous alignment of the five spacecraft near 2300 LT and 11 R_E and within 1.5 R_E of the current sheet center, latitudinal gradients are analyzed. A significant latitudinal pressure gradient is present indicating the necessity of a $(J \times B)_z$ force to maintain the pre-onset equilibrium state. During thinning the total pressure remained approximately constant at all spacecraft rather than increasing. Within the plasma sheet, magnetic field strength increased while plasma pressure decreased due to decreasing temperature. We present a comprehensive explanation for the relationship between the thinning, the stretched structure, and development of intense current density. Our analysis of this event suggests that (1) the thinning in this event is an MHD force-balanced self-evolving process and is not a forced process due to an increased lobe field; (2) the thinning changes flux tube structure in length and curvature but not significantly in volume; (3) the thinning evolves with a change of the radial plasma pressure profile in the near-Earth tail, which is associated with a locally intensified current sheet. The conclusion is that the increased lobe field strength is not the necessary and the primary cause for cross tail current sheet thinning but rather thinning can occur within the plasma sheet as a result of unknown internal processes.

Citation: Saito, M. H., D. Fairfield, G. Le, L.-N. Hau, V. Angelopoulos, J. P. McFadden, U. Auster, J. W. Bonnell, and D. Larson (2011), Structure, force balance, and evolution of incompressible cross-tail current sheet thinning, *J. Geophys. Res.*, 116, A10217, doi:10.1029/2011JA016654.

1. Introduction

[2] The cross-tail current sheet exists in the magnetotail as a permanent feature, and it exhibits both slow and rapid temporal variations. Thinning of the plasma sheet and the embedded current sheet is revealed as an increasing magnetic pressure, and such thinning is known as a typical harbinger of substorm onset in the magnetotail [e.g., *Nishida and Hones, 1974; Nagai et al., 1997*]. These tail signatures led to the widely accepted scenario that the thinning of the plasma/current tail is a signature of energy-transfer from solar wind into the magnetosphere caused by compression of the lobe field. In the event described below we will describe a

small substorm where thinning occurs in the absence of an increasing lobe field strength: an observation that suggests that an internal plasma sheet process leads to a formation of a weak equatorial field that may be susceptible to an instability.

[3] The conventional picture for thinning and its relationship to a substorm is as follows. Southward turning of interplanetary magnetic field enhances magnetic reconnection and polar cap convection as magnetic field lines are transported to the nightside magnetosphere, increasing the magnetic flux and the diameter of the tail [*Maezawa, 1975*]. An increased component of the solar wind pressure normal to more flared magnetopause compresses the tail and creates the thinned current sheet. The thinned current sheet is thought to be susceptible to magnetic reconnection and substorm onset. This picture is invoked as our conventional understanding of growth phase of substorm and has been modeled extensively. Still processes within the plasma sheet have not been fully revealed nor theoretically explained. One of the critical and unanswered question is how a global magnetospheric convection of flux transport leads to the evolution of the plasma sheet and finally form a weak field regions or a near-Earth neutral line at $X = -10$ to $-30 R_E$.

¹NASA Goddard Space Flight Center, Greenbelt, Maryland, USA.

²Institute of Space Science, National Central University, Jhongli, Taiwan.

³Institute of Geophysics and Planetary Physics, University of California, Los Angeles, California, USA.

⁴Space Science Laboratory, University of California, Berkeley, California, USA.

⁵Institut für Geophysik und Extraterrestrische Physik der Technischen Universität Braunschweig, Braunschweig, Germany.

[4] *Erickson and Wolf* [1980] investigated the adiabatic compression of a magnetotail flux tube convecting earthward and found that this will result in a greatly enhanced pressure in the near-Earth tail. Since such pressures are not observed, it was concluded that sunward convection must be an unsteady process. Later, *Hau et al.* [1989] and *Hau* [1991] constructed a steady force-balanced MHD model in which the magnetotail has a broad minimum in the equatorial magnetic field strength in the near-Earth plasma sheet. In such a model, steady convection becomes possible. Such a profile has been found to be maintained persistently before the substorm onset [*Saito et al.*, 2010], proving observational support of the idea that B_z evolves in a manner that the excess pressure issue is avoided. During the growth phase, intense cross-tail current density is required in the near-Earth tail to account for the observed increasingly stretched field [*Kaufmann*, 1987]. It is often speculated that increasing plasma pressure due to enhanced convection may account for the increase of the cross-tail current density [e.g., *Zaharia and Cheng*, 2003].

[5] To better understand the physics within the plasma sheet, we tentatively suggest that during plasma sheet thinning the following changes may or may not be observed: an increase in the lobe field strength, the development of plasma pressure gradient in radial direction, and the formation of the weak field region. A deepening minimum B is consistent with observations of high beta values of 50 just prior to onsets [*Lui et al.*, 1992; *Saito et al.*, 2008] which may importantly influence substorm onset physics. See *Samson and Dobias* [2005] for a high beta disruption scenario. A similar scenario emphasizing the role of the high beta on closed field lines has also been suggested for solar flares [*Shibasaki*, 2003]. The stability of 2D (x, z) magnetotail in a high beta plasma has been examined both theoretically and numerically by various authors studying the ballooning instability [e.g., *Miura et al.*, 1989; *Lee and Wolf*, 1992; *Hurricane*, 1997; *Pu et al.*, 1997; *Bhattacharjee et al.*, 1998; *Cheng and Lui*, 1998; *Horton et al.*, 2001; *Zhu et al.*, 2007; *Pritchett and Coroniti*, 2010; *Raeder et al.*, 2010] and also the tearing instability [*Sitnov and Schindler*, 2010]. Collisionless plasmas in inhomogeneous magnetic fields are subject to various kinetic effects such as bounce motion of particles. These effects impose a low frequency limit for the applicability of fluid or MHD description [*Pellat et al.*, 2000; *Le Contel et al.*, 2000a, 2000b]. Such a fluid or MHD description of the ballooning instability is not a priori valid for magnetotail plasma but is likely a posteriori verified for the model magnetotail of $|X| < 15 R_E$ for modes with a growth rate larger than the ion bounce frequency [*Miura*, 2004].

[6] It has been difficult to study the event-to-event variations and the temporal evolution of the spatial profiles of plasma sheet changes using a single spacecraft measurement. However, if we have multipoint measurements which allow us to examine the gradient of both field and plasma, we can track changes of spatial structures in 2D (x, z) geometry as follows. The tail plasma sheet in a quasi-steady slow-flow state may be approximated by the MHD force balance equation [cf. *Kaufmann et al.*, 1997]

$$\nabla P = \mathbf{J} \times \mathbf{B} \quad (1)$$

where P is plasma pressure, \mathbf{J} is current density, and \mathbf{B} is magnetic field. Noting the vector identity $2\mathbf{B} \times (\nabla \times \mathbf{B}) = \nabla B^2 - 2(\mathbf{B} \cdot \nabla)\mathbf{B}$ where $B = |\mathbf{B}|$, equation (1) can be written into the relationship between total pressure P_t and magnetic field structure:

$$\nabla P_t = \mu_0^{-1}(\mathbf{B} \cdot \nabla)\mathbf{B} = 2P_b \mathbf{K} \quad (2)$$

where $P_b = B^2/2\mu_0$ is the magnetic pressure, $\mu_0 = 4\pi \times 10^{-7} \text{ Hm}^{-1}$ and \mathbf{K} is the curvature of the magnetic field defined by

$$\mathbf{K} = \frac{(\mathbf{B} \cdot \nabla)\mathbf{B}}{B^2} \quad (3)$$

Measurements of the gradient in total pressure will provide the curvature of a magnetic field line. From equation (1), $(\mathbf{J} \times \mathbf{B}) \perp \mathbf{B}$, we also obtain the expression

$$\mathbf{B} \cdot \nabla P = 0 \quad (4)$$

In MHD force-balanced conditions, plasma pressure is constant along a magnetic field line. A plasma pressure obtained at a distance from the equator can be extrapolated to the equator along magnetic field lines.

[7] Equatorward motion of the aurora is frequently observed before a substorm onset. It is natural to expect that thinning of the current/plasma sheet and its associated earthward motion is a corresponding signature in the magnetotail for this slow change. Obtaining the spatial profile at the magnetic equator is important for solving the long-standing mapping problem between the ionosphere and magnetosphere. According to the Vasyliunas equation which may be derived from equation (1) [*Vasyliunas*, 1970; *Zaharia and Cheng*, 2003]:

$$\frac{J_{\parallel}}{B} = \frac{\mathbf{B}_{\text{eq}}}{B_{\text{eq}}^2} \cdot (\nabla V \times \nabla P_{\text{eq}}) \quad (5)$$

where V is the magnetic flux tube volume per unit flux. The left hand side and the right hand side are the quantities in the ionosphere and in the magnetosphere, respectively. The field-aligned current in this equation is due to the three-dimensional geometry of the plasma sheet where adjacent flux tubes support different magnitude of the perpendicular currents in the equilibrium. The equatorward motion of aurora during the growth phase may be mapped to the changes of the equatorial profile of plasma pressure P or the magnetic flux tube volume per unit flux V .

[8] This study is concerned with the structure and force balance of the current sheet observed near-Earth ($X \sim -11 R_E$) before and during the thinning of the tail plasma sheet. We will explain how the thinning of the tail, which occurs without an increase in lobe field strength, is related to the formation of intense current density and formation of a weak field region in the near-Earth tail. Section 2 presents the model and parameters computed from gradient measurements. Section 3 discusses the result and their physical meanings that are

relevant to plasma behaviors during thinning, the formation of the current sheet, the structure of flux tube, and equatorward motion of aurora. Section 4 summarizes the conclusions.

2. Model and Equations for Analysis

2.1. Model Assumptions

[9] Any parameter A with spatial variation along a given direction can be obtained by two-point measurements along that direction in a local Cartesian system:

$$\Delta A = \frac{\partial A}{\partial r} \Delta r + \frac{\partial A}{\partial \phi} \Delta \phi + \frac{\partial A}{\partial z} \Delta z \quad (6)$$

where $\partial A/\partial r$, $\partial A/\partial \phi$, and $\partial A/\partial z$ represent actual spatial variations. In this study, we examine the thin plasma sheet observed by multiple spacecraft with separations of $\Delta r \sim \Delta \phi \sim \Delta z$. When the spacecraft have similar r and ϕ positions, we may assume the pronounced z variations and locally two-dimensional geometry:

$$\left| \frac{\partial A}{\partial z} \right| \gg \left| \frac{\partial A}{\partial r} \right| \quad (7)$$

$$\frac{\partial A}{\partial \phi} \simeq 0 \quad (8)$$

The above assumptions are applicable to a thin current sheet geometry observed for the event to be studied here and previously shown by *Saito et al.* [2010], who examined the spatial profiles of the magnetic field. Both radial and z components of the magnetic field are well ordered by the z position of the five spacecraft, while they are not well ordered by r and ϕ . Under these assumptions, we obtain the latitudinal (Z) gradient.

2.2. Equations for Analysis

[10] When gradient is available for only one direction z , two points at z_i and z_j separated by $\Delta z = z_i - z_j$ give the gradient at $z_c = (z_i + z_j)/2$. The pressure gradients are

$$\nabla_z P = \frac{\Delta P}{\Delta z} \quad (9)$$

$$\nabla_z P_t = \frac{\Delta P_t}{\Delta z} \quad (10)$$

The cross-tail current density and latitudinal component of the $\mathbf{J} \times \mathbf{B}$ force are calculated as follows. The radial gradient is not obtained, but we assume it is negligible, which should be approximately true in thin geometry. The cross-tail current density is given by

$$J_{\perp} = \frac{1}{\mu_0} \left(\frac{\partial B_r}{\partial z} - \frac{\partial B_z}{\partial r} \right) \quad (11)$$

which can be approximated by

$$J_{\perp, approx.} = \frac{1}{\mu_0} \frac{\Delta B_r}{\Delta z} \quad (12)$$

Similarly,

$$\begin{aligned} (\mathbf{J} \times \mathbf{B})_z &= \frac{1}{\mu_0} (J_x B_y - J_y B_x) \\ &= \frac{1}{\mu_0} \left(B_y \frac{\partial B_z}{\partial y} - B_y \frac{\partial B_y}{\partial z} - B_x \frac{\partial B_x}{\partial z} + B_x \frac{\partial B_z}{\partial x} \right) \end{aligned} \quad (13)$$

$$(\mathbf{J} \times \mathbf{B})_{z, approx.} = \frac{1}{\mu_0} \left(-B_y \frac{\Delta B_y}{\Delta z} - B_x \frac{\Delta B_x}{\Delta z} \right) \quad (14)$$

Assuming the latitudinal MHD force balances, the latitudinal component of the magnetic field line curvature is estimated from the total pressure gradient from equation (2):

$$K_z = \frac{\nabla_z P_t}{2P_b} \quad (15)$$

The definition of the field line curvature by equation (3) is different from the one $\mathbf{k} = (\mathbf{b} \cdot \nabla)\mathbf{b}$, where $\mathbf{b} = \mathbf{B}/B$, however they are related by

$$2P_b \mathbf{K} = 2P_b \mathbf{k} + \frac{1}{\mu_0} (\mathbf{B} \cdot \nabla) \mathbf{B} \quad (16)$$

They represent qualitatively the same field line structure only when the second term of the right hand side is negligible and will not change the sign of the z component of the curvature vector. The deduced radius from equation (15), therefore, requires caution when reconstructing the actual field line structure based on that radius when significant presence of the gradient in the magnetic field strength.

3. Results and Discussion

[11] This analysis uses THEMIS spacecraft data from the substorm event on April 8, 2009 studied by *Saito et al.* [2010]. All five THEMIS probes [*Angelopoulos, 2008; Frey et al., 2008*] in formation flight with identical instrumentation are used to reveal the latitudinal profile of the current sheet. The magnetic field data are from the fluxgate magnetometers on 2 m booms [*Auster et al., 2008*]. Though their sampling rate is as much as 64 Hz, we use averaged values over 3 s and 5 min. The plasma distributions are calculated by combining Electrostatic Analyzers (ESA) [*McFadden et al., 2008a*] and Solid State Telescopes (SST) data. See appendix for further details on the plasma moment calculation.

3.1. The Event and Probe Alignment

[12] Figure 1 shows THEMIS five-spacecraft time series data of their locations in Geocentric Solar Magnetospheric System or GSM (thick) and Solar Magnetic or SM (thin dashed) coordinate systems and magnetic field observations in GSM coordinates from 6 to 8 UT during the substorm on April 8, 2009. THEMIS probes, P1, P2, P3, P4, and P5 were located from north to south in this order, all within $1.5 R_E$ of the magnetic equator near $X \sim -11 R_E$ and $Y \sim 4 R_E$. Probes P1 to P4 were located in the northern hemisphere with P4 being the closest to the magnetic equator. The probe locations of X and Y are virtually identical in both coordinates. Owing to the dipole tilt angles of $-2.6, -1.4$

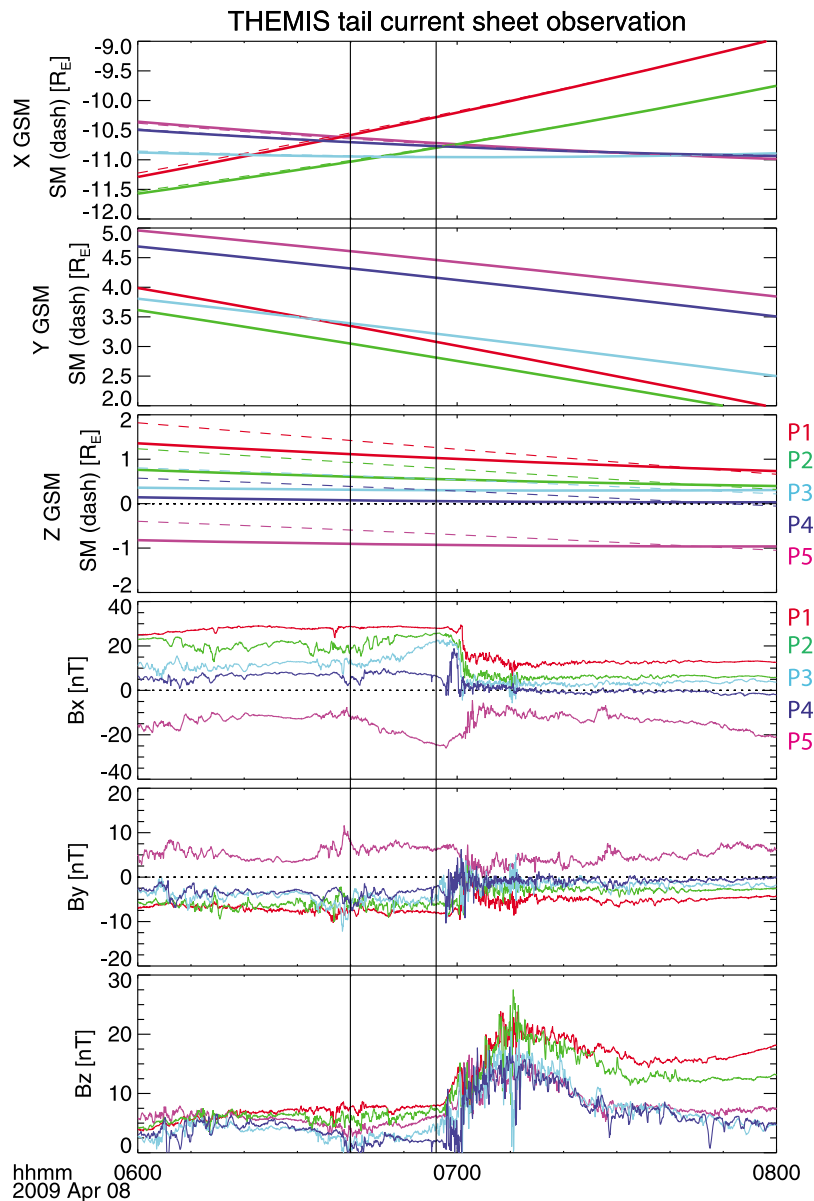


Figure 1. Locations and magnetic field data during the April 8, 2009 substorm observed by five THEMIS spacecraft. Each color represents values at each probe: P1 (red), P2 (green), P3 (cyan), P4 (blue), and P5 (magenta). Two vertical lines indicate the interval during thinning (06:40–06:56 UT).

and 0.25 degrees for 6 UT, 7 UT and 8 UT, respectively, Z locations show slight differences which vary as function of time. The THEMIS dipolarization at ~ 0700 UT corresponded to a small substorm onset with a negative H perturbation at Snap Lake at 71 degrees magnetic latitude that was near the 2300 MLT of THEMIS. The maximum depression of 180 nT was much larger than that at any other observatory and it was the only perturbation during a very quiet day. The IMF was very weak with $B_z \sim -1$ nT in GSM with almost constant solar wind dynamic pressure of 2 nPa.

3.2. Observation Results

[13] Figure 1 includes the interval before and during the thinning of the cross-tail current and the time after the dipolarization onset. The interval of interest in this study between

6 and 7 UT has been previously studied by *Saito et al.* [2010]. They analyzed the spatial profile of B_z and found the formation of a magnetic field minimum from 0640 UT to 0656 UT. This is also the interval before the dipolarization onset at 0656 UT when the magnetic field data indicated thinning of the current sheet. This current sheet thinning was seen by probes P2, P3, and P5 which showed a systematic increase of $|B_x|$ from 0640 UT (first vertical line) to 0656 UT (second vertical line). It is significant that such a $|B_x|$ increase was absent for P1 in the outer most part (farther from the equator) of the current sheet and P4 in the inner part (closer to the equator). This magnetic behavior is not consistent with the idea that the thinning is caused by the increase of the lobe field strength. This point will be further investigated with plasma data and will be elaborated below.

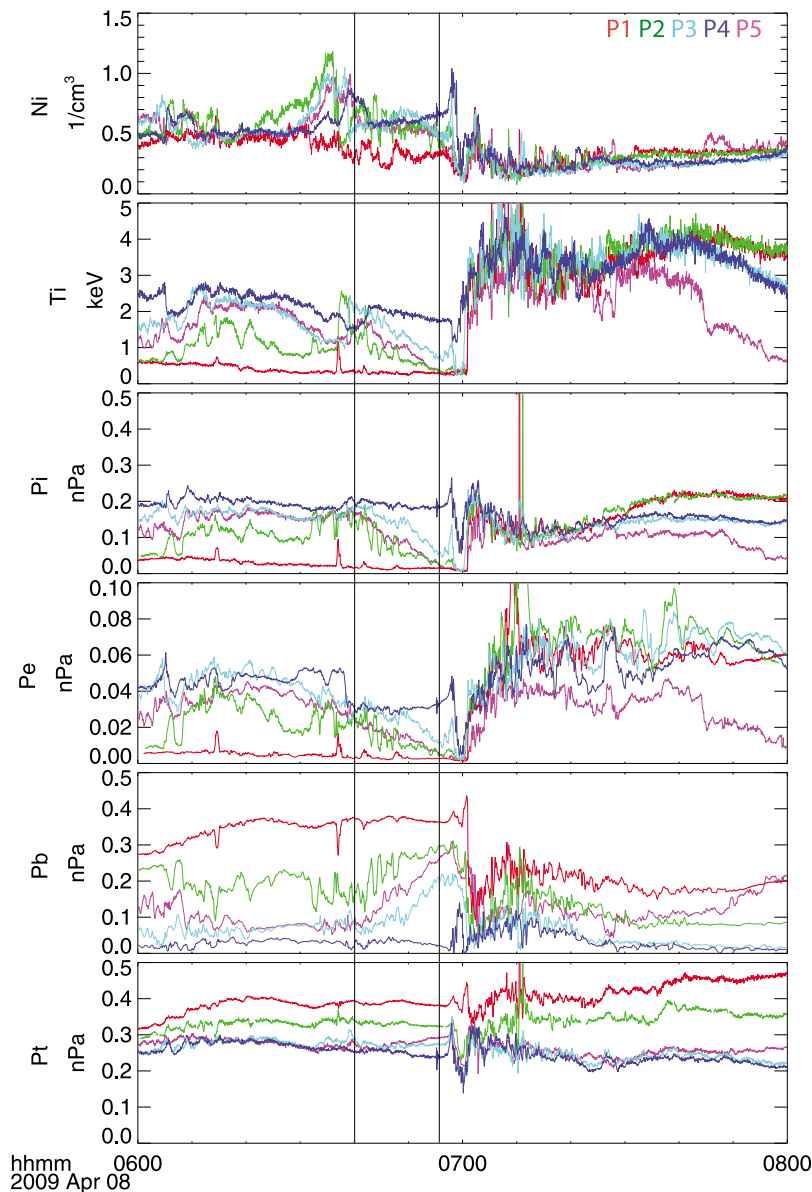


Figure 2. Ion density, temperature and ion, electron, magnetic, and total pressures for five probes. Each color represents values at each probe. Colors and vertical lines are the same as Figure 1.

[14] Figure 2 shows temporal evolution of the calculated plasma and magnetic parameters for the five probes for the same intervals as Figure 1. The colors are the same format used for Figure 1. Before the dipolarization onset at 0656 UT, the ion and electron pressures P_i and P_e at various locations depend on their relative distance from the center of the plasma sheet. It should be noted that the behavior of various parameters suggest that this center is actually located at about $0.2 R_E$ south of the solar magnetospheric equator and the relevant spacecraft positions are between the solar magnetic and solar magnetospheric positions in Figure 1. These assumptions explain why P1 pressure is larger than P5, why P3 pressure is greater than P5, and why B_x at P4 is significantly positive. Similarly, magnetic pressures P_b , which are primarily due to the radial component of the magnetic field, also vary with respect to the center of the current sheet in an

inverse manner. On the other hand, plasma density depends less on location both before and during the thinning.

[15] The thinning of the tail current sheet observed by P2, P3, and P5 was associated with an increase of the magnetic pressure and a decrease of the plasma pressure, keeping the total pressure $P_t = P_b + P_i + P_e$ approximately constant. Therefore the thinning cannot be explained simply as a consequence of the increased magnetic field strength in lobe. Note that there was no increase in plasma pressure observed during the thinning. This indicates the intense current cannot be explained simply by pressure build up due to enhanced convection, which is thought to result in the increase of plasma pressure at the earthward edge of the plasma sheet. The decrease of plasma pressure observed by P2, P3, and P5 during thinning was due to the decrease of temperature, while density was weakly variable both in time and in

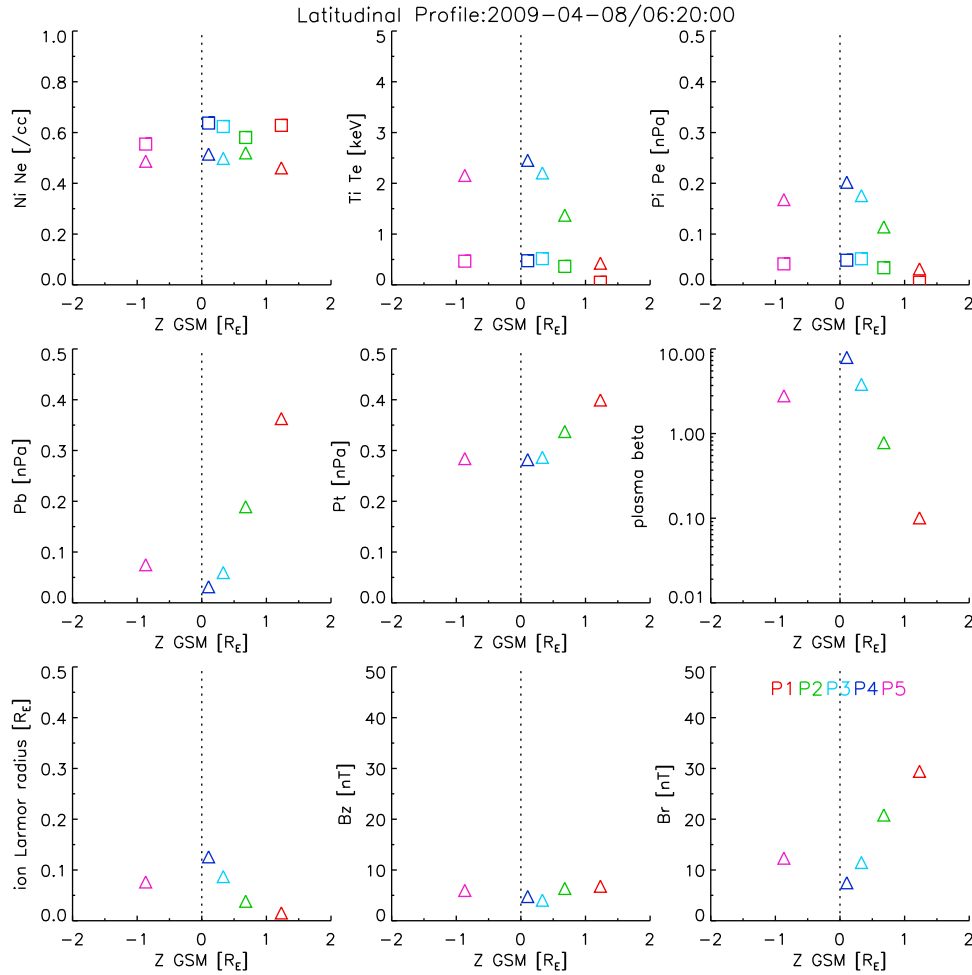


Figure 3. Plasma and magnetic parameters as a function of latitudinal location averaged for a 5 min interval centered at 06:20 UT. These data represent latitudinal profiles before the thinning of the current sheet.

location. The temporally constant density indicates that the plasma in the tail is incompressible during the thinning of the cross-tail current.

[16] The total pressures stayed almost constant in time for each probe, but probes P1 and P2 with a Z separation of $\sim 0.5 R_E$ exhibited a significant difference implying a significant gradient in outer current sheet both before and during the thinning of the tail. The inner probes P3 and P4 with a Z separation of $\sim 0.2 R_E$ showed no gradient in total pressure at the inner part of the current sheet before the thinning but showed a gradient during the thinning. In quasi-static MHD force-balanced state, the gradient in total pressure implies a tension force of the curved field lines (equation 15), which means that the change of total pressure gradient indicates a change of the flux tube structure.

[17] Figures 3 and 4 illustrate spatial profiles of the current sheet at 0620 UT and at 0650 UT respectively which represent characteristics before and during the thinning. The spatial profiles are constructed from 5-min averages of the various parameters, which are plotted versus probe locations in Z . Figures 3 and 4 show that parameters are well ordered by Z , being consistent with the thin tail-geometry approximation. The top panels show densities, temperatures, and

pressures for ions (triangles) and electrons (squares). The approximately 20% differences between electron and ion density measurements in Figures 3 and 4 attribute to errors in both ion and electron detection system. The ion density observations can be affected by background count and the assumption that all ions are protons [McFadden *et al.*, 2008b], while the electron density observations suffer the effects of photoelectrons and secondary electrons. The middle panels show magnetic pressure, total pressure, and plasma beta. The bottom panels show Larmor radii of the thermal ions, the normal magnetic field components B_z , and the radial magnetic field components $B_r = \sqrt{B_x^2 + B_y^2}$. As noted earlier and as can be seen in Figures 3 and 4, the spatial profile of B_r is symmetric about the magnetic equator located at $Z \sim -0.2 R_E$ in GSM.

[18] The plots of B_r and B_z versus Z were used for examining the validity of the thin geometry approximation of the model by Saito *et al.* [2010]. Various plasma parameters shown in Figures 3 and 4 also confirm that the spatial profiles in Figures 3 and 4 can be regarded as the latitudinal profiles of the current/plasma sheet at $X = -11 R_E$ and $Y = -4 R_E$ for the intervals before and during the thinning

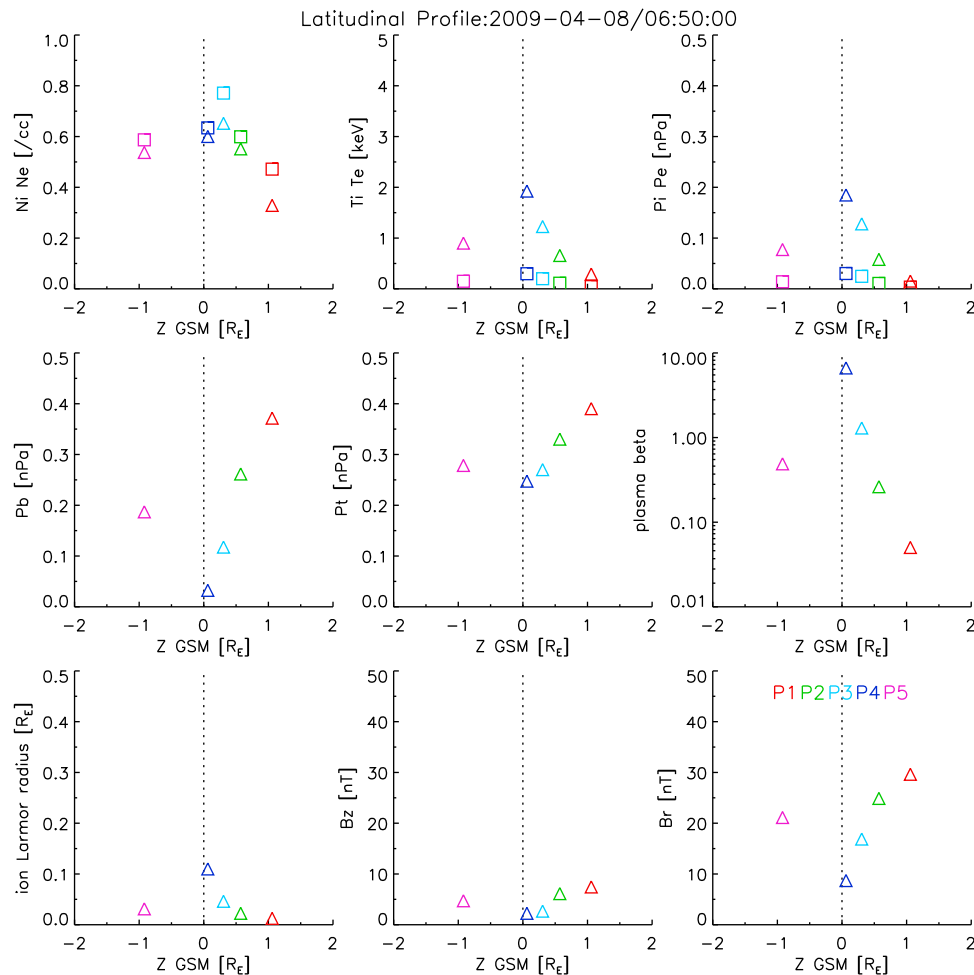


Figure 4. Same as Figure 3 except for during thinning of the current sheet at 06:50 UT.

of the tail, respectively. Density was found to be weakly dependent on the latitudinal locations, while plasma and magnetic pressures showed clear spatial variation that is consistent with an equilibrium current sheet. The spatial profiles of the total pressure show that there is a systematic gradient, indicating that the flux tube geometry has at least 2D geometry.

[19] Figure 5 shows temporal evolution of parameters derived from the latitudinal gradients from 6 UT to 7 UT. We use the four THEMIS probes P1, P2, P3, P4 in the northern hemisphere to obtain the gradient at three center positions within the current sheet. Figure 5a shows the three locations where the gradients were obtained using P1 and P2 (green), P2 and P3 (cyan), and P3 and P4 (blue). Figure 5b shows the cross-tail current density using equation (12). In the late stage of the thinning, there was an enhancement of cross-tail current at the innermost location (blue), while the outer part did not show significant increase. Figures 5c and 5d show latitudinal forces given by equation (9) and equation (14). At the inner most part of the current sheet, the negative values of both quantities increased as the cross-tail current density developed. Figure 5e shows that their difference was small for the whole interval, meaning that the MHD force balance is maintained throughout the interval. Figures 5f and 5g show the magnetic tension forces and the

curvature of the magnetic field line given by equations (10) and (15) respectively. Caution should be exercised in interpreting the curvature in Figure 5g which is based on the tension force in Figure 5f (see equation 15). When the magnetic tension force is nearly zero (dark blue dotted line from 0600 UT to 0630 UT), the curvature in Figure 5g is not reliable. In addition, when there is fluctuation in velocity (from 0630 UT to 0645 UT), both the tension force and the curvature are not reliable due to a lack of the MHD force balance (see next section for this explanation). As we have seen in Figure 2, all panels in Figure 5 show that the innermost part of the current sheet (blue) and the outer part of that (green and cyan) behaved differently. The quantities in outer part of the current sheet were stable both before and during the thinning. The magnetic field tension force (Figure 5f) in the inner part of the current sheet was negligible before the thinning and became significant during the thinning.

[20] A novel aspect of this analysis is the calculation of current densities and gradients using the small differences in measured quantities at nearby spacecraft divided by their spatial separations. In dealing with such differences the accurate intercalibration between the identical instruments on the different spacecraft is particularly important. In particular, any measurement errors between spacecraft, when divided by the small spatial separations, should be smaller

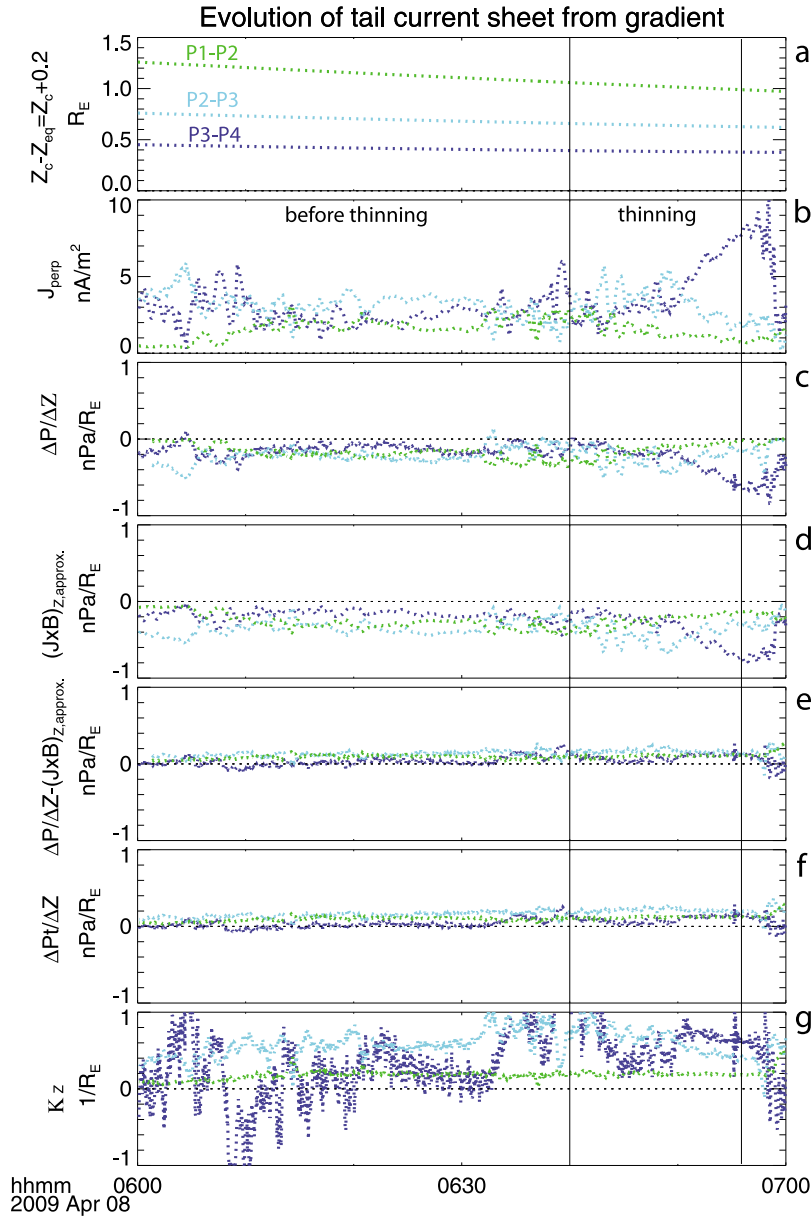


Figure 5. Properties of the current sheet. Two vertical lines are the same as in Figure 1. Current sheet parameters are derived from the latitudinal gradients. See text for details.

than the actual gradients. It is difficult to quantify the errors but the experimenters have expended considerable effort comparing data during close encounters at quiet times in order to minimize such errors. The best evidence of their success is probably a posteriori verification of the assumptions used in this study which lead to results such as the approximate balance between the pressure gradient and $\mathbf{J} \times \mathbf{B}$ forces in Figures 5c and 5d.

3.3. Validity and Applicability of MHD Force Balance

[21] As discussed in introduction, the MHD force balance equation is expected to be a basis for describing the quasi-static slow-flow state of the plasma sheet during the growth phase. Our analysis provided observation-based validity of MHD force balance in the near-Earth tail for the first time, using the latitudinal components of ∇P and $\mathbf{J} \times \mathbf{B}$

forces. We note that this is not a both observationally and theoretically obvious issue, though a set of MHD equations with an adiabatic closure equation has been widely used as a basis for understanding growth phase behavior as mentioned in introduction. The presence of the low-frequency limitations of the fluid and MHD approach has been pointed out for collisionless plasmas confined by magnetic field. The slowly evolving plasma sheet may be subject to kinetic effect, which arises from bounce motions of particles. A condition for a small fraction of resonant particles requires a low frequency limit for the validity of MHD. A self-consistent kinetic approach is required for the plasma sheet [Pellat *et al.*, 2000; Le Contel *et al.*, 2000a, 2000b]. When the curvature radius of the magnetic field line is of the order of the Larmor radius of particles, the adiabatic invariants are not conserved. Isotropization by pitch angle scattering due to the curvature

effect allows to perform an averaging over the pitch angle or the magnetic moment [Hurricane *et al.*, 1995]. In this stochastic regime, some MHD behaviors of the low-frequency perturbation of the magnetotail could be recovered in spite of the strong kinetic effects and can be called MHD-like evolution [Hurricane *et al.*, 1995].

[22] For the above reasons, one may consider that the observed MHD force balance could be ostensible, for instance, the other forces arising from quasi-neutrality or non-linear effects may cancel each other so that the observable parameters resemble MHD or fluid behavior. In order to clarify whether the observed plasma sheet is in the adiabatic regime or the stochastic regime, further study is required to analyze magnetic field geometry together with kinetic characteristics. Though the present study does not guarantee validity of MHD for the plasma sheet in general, still the observation showed that two forces evolved in balance.

[23] Using the fact that MHD force balance is good approximation for the tail plasma sheet before substorm onset, we can deduce the larger-scale structure of a flux tube and the radial profile of pressure. In addition, the force balance condition can be used to reconstruct the field line structure by using the total pressure gradient. During tail current sheet thinning, there were systematic increases of both forces. Their difference is seen to be small both before and during the thinning. It is seen that their difference in Figure 5e ($\Delta P/\Delta Z - (\mathbf{J} \times \mathbf{B})_{z,approx.}$) and the total pressure gradient in Figure 5f show very similar values and temporal evolution. Below we will argue that this is not due to the imbalance of the MHD forces.

[24] First, their similarity can be understood by considering the following two equations:

$$(\nabla P)_z - (\mathbf{J} \times \mathbf{B})_{z,approx.} = B_x \frac{\partial B_z}{\partial x} + B_y \frac{\partial B_z}{\partial y} - nm \frac{dv_z}{dt} \quad (17)$$

$$\nabla_z P_t = (\mathbf{B} \cdot \nabla) B_z - nm \frac{dv_z}{dt} = B_x \frac{\partial B_z}{\partial x} + B_y \frac{\partial B_z}{\partial y} + B_z \frac{\partial B_z}{\partial z} - nm \frac{dv_z}{dt} \quad (18)$$

Equations (17) and (18) suggests what we see in Figures 5e and 5f respectively. From equation (17) one can see that most of the observed difference between two forces ∇P and $\mathbf{J} \times \mathbf{B}$ in Figure 5e can be primarily attributable to the approximate expressions for the $(\mathbf{J} \times \mathbf{B})_z$ term and the imbalance of MHD forces $nm dv_z/dt$. From equation (18), one can see that the total pressure gradient is equal to the magnetic tension force if $nm dv_z/dt$ is negligible, and one can see the similarity of the right hand sides of equation (17) and (18). Since the only difference is the term $B_z \partial B_z / \partial z$ between equations (17) and (18), they showed similar temporal evolution.

[25] Second, MHD force balance or negligible $nm dv_z/dt$ can be a good assumption and appropriate description of the data, if both $|\partial \mathbf{v} / \partial t|$ and $|(\mathbf{v} \cdot \nabla) \mathbf{v}|$ are much smaller than $|\nabla P|$. Figure 6 shows velocity data from 6 UT to 7 UT for all probes. The absolute value of $|\mathbf{v}|$ was also small compared with both Alfvén velocity and sound velocity v_s during the most of the interval. Though there were some variations in velocity for short intervals, there were no systematic temporal changes in \mathbf{v} , which could contribute to significant

$|\partial \mathbf{v} / \partial t|$. $|(\mathbf{v} \cdot \nabla) \mathbf{v}|$ is roughly estimated to be 2% of $|\nabla P|$ if $|\mathbf{v}| = 0.1 v_s$.

[26] In order for ∇P_t to be an accurate magnetic tension force, $|\mathbf{v}|$ needs to also be smaller than the Alfvén velocity v_a so that $|(\mathbf{v} \cdot \nabla) \mathbf{v}|$ is negligible compared with $|(\mathbf{B} \cdot \nabla) \mathbf{B}|$. At probe P4, which was relatively near the magnetic equator, $|(\mathbf{v} \cdot \nabla) \mathbf{v}|$ may not be negligible so that quantitative assessment of the deduced curvature requires caution. Still the deduced sign of the curvature is apt to be valid.

3.4. Physical Implications

[27] We analyzed the fortuitous encounter of the near-Earth tail current sheet by 5 THEMIS spacecraft which allow determination of the latitudinal profiles of the current sheet and how they evolve with time prior to substorm onset. This temporal evolution can be divided into two parts: before the thinning and during the thinning of the tail current sheet. The backbone of the analysis methodology here is utilization of the tail approximation where latitudinal variations are much larger than radial variations. This assumption is less restricting than the commonly employed assumption of 1D or Harris-type geometry and can be applicable to other current sheet analyses. Latitudinal profiles of the current sheet enabled us to deduce important parameters such as current density, MHD forces, etc. for understanding the evolution of the current sheet.

3.4.1. Thinning of the Tail and Pressure Evolution

[28] The thinning of the current sheet is identified by a gradual increase of the radial or $|B_x|$ components of the magnetic field. This increase was observed by three of the five probes, P2 P3 and P5 from 0640 UT to 0656 UT. The timescale of 20 min is consistent with the typical timescale for auroral equatorward motion before the substorm onset [Liu *et al.*, 2007]. The static states before the thinning and during the thinning are separated by a several minute transition interval with noticeable field and particle fluctuations. This increase of $|B_x|$ was only observed $\sim 1 R_E$ from the magnetic equator. It is noteworthy that the outermost probe did not detect the magnetic field signature of the thinning, which is contrary to the general idea that the tail thinning is associated with an increasing lobe field strength. This contradiction is further supported by the fact that at a given location of the current sheet, the total pressure remained almost unchanged as the thinning of the tail proceeded.

[29] The general picture of the increase of the lobe field being the cause of the thinning of the tail came from magnetic field measurements by single spacecraft [e.g., Fairfield and Ness, 1970]. Though our multipoint study of one event produces counterevidence, the generality of this behavior requires further study focusing on event dependence between smaller substorms and larger substorms. Other factors may be location dependence in radial distance from Earth and local time. Nagai *et al.* [1997] reported Geotail observations of a clear increase of both plasma and magnetic pressure in the plasma sheet at 20–50 R_E during the substorm growth phase for 15 events out of 19. They selected substorms after clear southward tunings of IMF B_z to clarify the relationship with the tail compression, while our event occurred during weak IMF and almost constant solar wind dynamic pressure. Nagai *et al.* [1997] showed that the increases in the total pressure were mainly caused by increases in the plasma

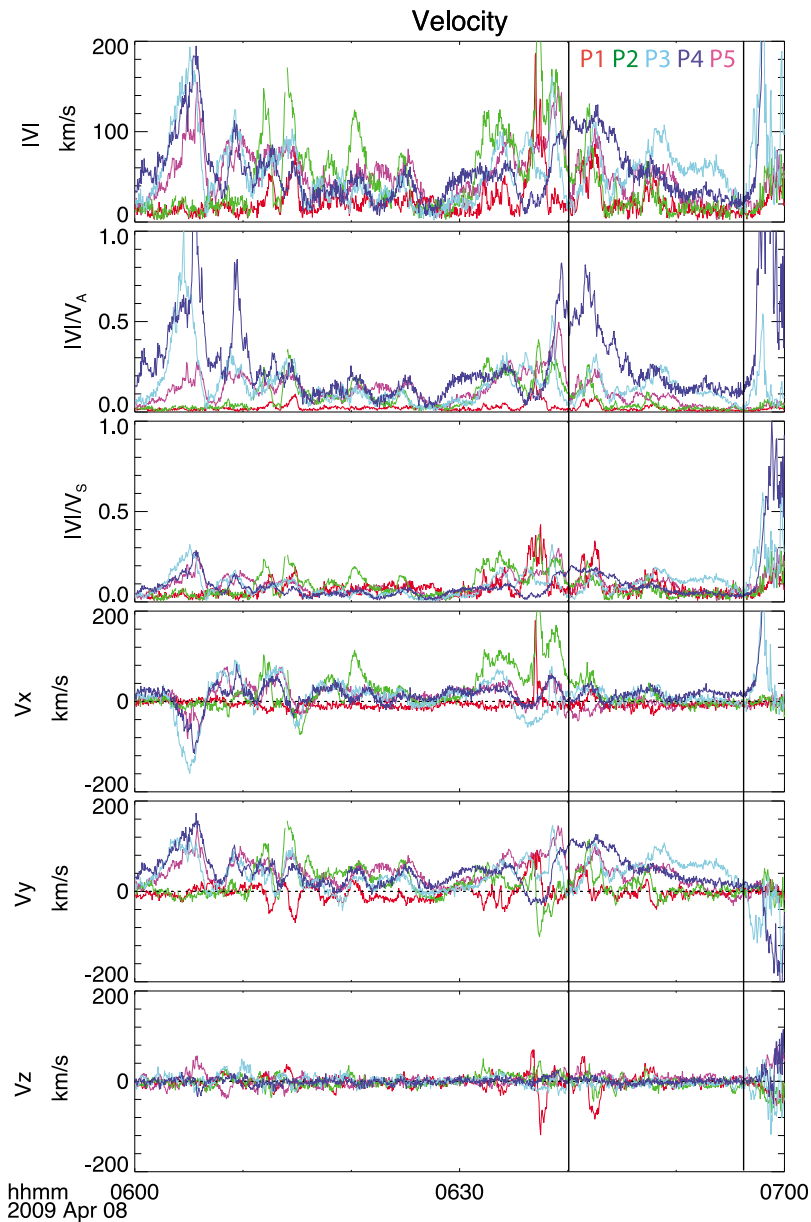


Figure 6. Velocities detected by all probes. The top three panels are the absolute value, followed by values normalized values by the Alfvén velocity and sound velocity respectively. The bottom three panels are three components in GSM coordinate. Colors and vertical lines are the same as Figure 1.

sheet density whereas our event did not show a systematic increase of the plasma density.

[30] Another noteworthy observation in our study is a significant latitudinal gradient in total pressure and its evolution. While all probes were located within $1.5 R_E$ of the magnetic equator, the total pressures varied from 0.25 nPa to 0.4 nPa with increasing distance from the magnetic equator. This is consistent with statistical results from Geotail observations for quiet times and growth phases of substorms [Wang *et al.*, 2004]. In a quasi-static state, presence of a gradient in total pressure means the geometry of current sheet is not a 1D structure and the curvature of a flux tube magnetic field line is not zero under the approximation of MHD force balance.

[31] In the course of thinning, all three probes between the outermost probe (P1) and the innermost probe (P4) observed systematic increases of magnetic pressure and decreases of plasma pressure while having almost unchanged total pressure. This decrease in plasma pressure was mainly caused by a decrease in plasma temperature. This plasma pressure decrease can be regarded as an inevitable effect from constraints of having constant total pressure and increasing magnetic pressure. The constant total pressure is consistent behavior in a quasi-static current sheet.

3.4.2. Development of Intense Cross-Tail Current Density

[32] Utilizing magnetic field measurements from four probes in the northern hemisphere, we computed cross-tail current density (Figure 5b) at $\sim 0.4 R_E$, $\sim 0.6 R_E$, and $\sim 1 R_E$

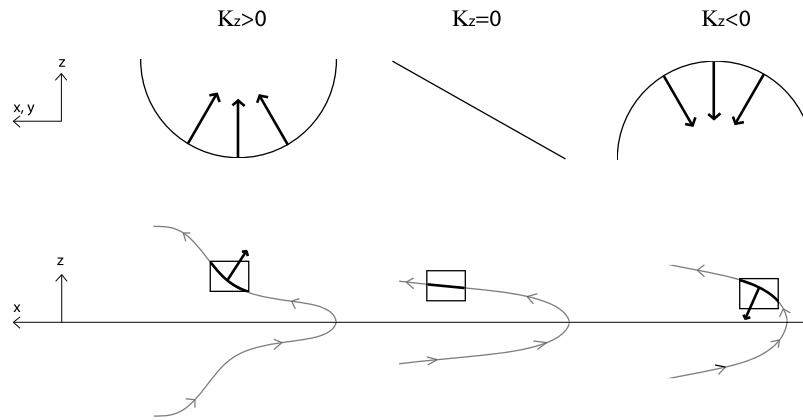


Figure 7. Sketch showing the sign of the curvature of the magnetic field line and the structure of the tail magnetic field flux tube where $|B_x| \gg |B_z|$ and $B_z > 0$ in the northern hemisphere of the thin tail geometry.

from the magnetic equator. For the most of the interval both before and during the thinning, the current density is larger at the inner location of the current sheet. In the outer part of current sheet, the current density was $1\sim 4$ nA/m², and stayed almost unchanged before and during the thinning. The inner part of current sheet, however, showed systematic increase up to 8 nA/m² late in the interval.

[33] In a two-dimensional model of the magnetotail [Kaufmann, 1987], the net dawn to dusk sheet current density integrated over the latitudinal direction I_y is given by

$$I_y = 2B_x/\mu_0 \quad (19)$$

where B_x is lobe magnetic field. This current closes with magnetopause current of $I_y/2$ at northern and southern hemispheres. Our observation of $B_x = 30$ nT yields $I_y = 48$ mA/m. There may be two scenarios for growth phase current depending on whether or not the lobe field increases: $\partial I_y/\partial t = 0$ and $\partial I_y/\partial t > 0$. The former is also consistent with an association of current/plasma sheet thinning with intensified current density. The current density evolution from 2 nA/m² to 8 nA/m² in a uniformly distributed profile implies a thickness changed from $4 R_E$ to $1 R_E$. Since the outer part of the current sheet density remained almost unchanged, the actual current profile must require an evolution that was structured to have constant net cross-tail current. In the latter case where the total current increases, the lobe field must increase before substorm onset, which was not observed here. Let us start with cross-tail current $I_y = 48$ mA/m for the time before the thinning. This 48 mA/m came from magnetopause current in the two magnetotail lobes with the strength 30 nT. The addition of 6 nA/m² current across the thickness of $0.8 R_E$ gives $I_y = 48$ mA/m + $(6$ nA/m² $\times 0.8 R_E) = 79$ mA/m, though it is not certain how this additional 31 mA/m could close within magnetosphere. This indicates assuming uniform current sheet profile may be wrong and a summation of locally calculated current densities will fail to observe the larger scale evolution of the current in the tail.

3.4.3. Changes of the Tail Structure

[34] The observed gradient in total pressure is taken as evidence for a magnetic tension force which enables the derivation of the curvature of the magnetic field line. Figure 7

shows the relationship between the sign of the latitudinal component of the curvature and its flux tube structure. From the sign of the curvature, the structure of a flux tube can be envisaged. Figure 7 (top) schematically shows the sense of curvature for positive, zero, and negative values of K_z . Figure 7 (bottom) places the curvature in a magnetotail context. For both before and during the thinning, the outer part of the current sheet remained unchanged, while only the inner part shows the structural changes illustrated schematically in Figure 8a. The relationship between a flux tube with intensified cross-tail current at the equator and its structure can be seen in model studies by Kaufmann [1987]. The flux tube with the intensified cross-tail current density has the positive curvature away from the magnetic equator and has stretched configuration. We draw in Figure 8a how the flux tube labeled with c changes from almost zero curvature on the left to the positive curvature configuration on the right.

[35] Additional information from the MHD force balanced condition is the radial profile of plasma pressure resulting from equation (4): plasma pressure is constant along the field line. In Figure 8a we also indicate plasma pressures with suffixes a, b, and c. They are observed by P1, P3, and P4, at the different distance from the magnetic equator but can be extrapolated along the magnetic field lines. The observed latitudinal profile can be used for estimating the radial profile at the magnetic equator. Our observation can be surmised in Figure 8b, which illustrates the qualitative changes for the radial profile of plasma pressure before and after the late stage of the thinning. Both the outermost and the innermost probes showed constant plasma pressure, while probes at $\sim 1 R_E$ from the center of the current sheet showed systematic decrease. At the later stage of the thinning of the current sheet, the steeper pressure gradient appeared in the near-Earth tail at $11 R_E$, which is consistent with interpreting the observed current density of 8 nA/m² as a diamagnetic current with pressure gradient scale of $\sim 2 R_E$.

[36] One may think that there is a discrepancy between the interpretation of the current density. For example, the measured ion V_y is about 100 km/s on P3 and with $n_i \sim 0.6$ /cc, which leads to an ion current density of about 10 nA/m². This is the order of the maximum deduced value of 8 nA/m² from this study. However, this ion V_y strongly decreases

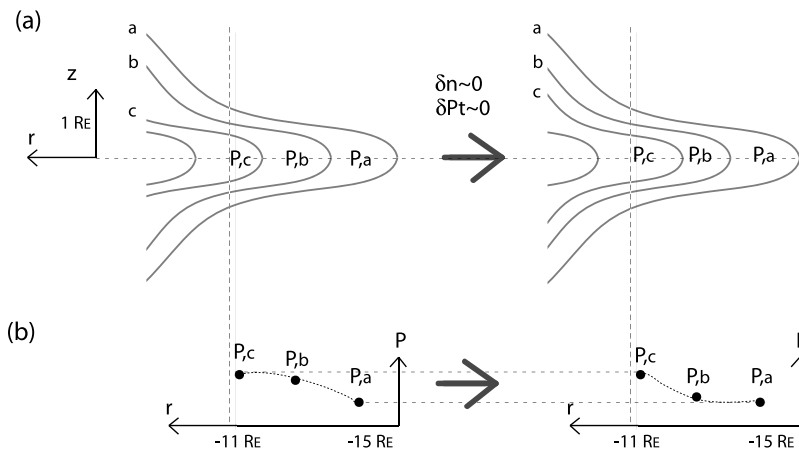


Figure 8. Sketch showing geometrical changes of three flux tubes a, b, and c at early and late stage of the thinning of the tail current sheet for (a) flux tube structures and (b) inferred plasma pressure variation along radial direction assuming MHD force balances. The reduction in pressure at P_b during thinning can be seen to increase the pressure gradient in the inner magnetotail. The separation between lines in Figure 8a does not indicate any information on the strength of the magnetic field.

as the perpendicular current is found to be maximum. The likely reason for this discrepancy is due to the fact that the measured V_y reflects both effect from $E \times B$ drift and ∇P drift. On the average and general sense, the direction of $E \times B$ drift is earthward in the midtail and downward at the innermost plasma sheet. However, it should be mentioned that we still do not completely understand the observed velocity evolution and their spatial variations.

3.4.4. Equatorward Motion of Aurora and Field-Aligned Current

[37] While the thinning of the tail current/plasma sheet is one manifestation of the growth phase of substorm, equatorward motion of aurora is an ionosphere manifestation that is likely the corresponding consequence of the thinning. It is expected that a field aligned current system moves earthward in the low latitude tail and equatorward in the higher latitude tail. The quasi-permanent Birkeland current can be understood from the Vasyliunas equation (equation 15) [Vasyliunas, 1970] and this current provides the link between currents into and from ionosphere and the plasma sheet profile in the equatorial plane.

[38] The earthward shift of region of the intense plasma pressure gradient may explain the equatorward motion of the Birkeland current system as modeled by Zaharia and Cheng [2003]. Our observed cross-tail current density of 8 nA/m^2 is consistent with that of 10 nA/m^2 in their model. As shown in Figure 8b, our observation shows the appearance of a pressure gradient region in the near-Earth tail. It should be stressed that it is not due to the increase in plasma pressure but due to the observed decrease in plasma pressure.

[39] Liu *et al.* [2007] elaborate that there are two scenarios for equatorward motion of aurora: 1) Earthward displacement of plasma which may lead to pressure buildup and 2) tailward stretching of field lines where nonadiabatic protons are pitch angle scattered by the small radius of the magnetic field line curvature closer to the Earth [Wanliss *et al.*, 2000]. The latter scenario was suggested to account for both equatorward motion and fading of proton aurora. Our multipoint analysis of this event strongly supports the latter scenario. Using the fact that the positive curvature was identified at

$0.4 R_E$ from the equator, we may make an estimation that the radius at the magnetic field line curvature at the magnetic equator is not larger than $0.4 R_E$. The normal magnetic field at the magnetic equator can be estimated to be in the order of 3 nT from the spatial profiles of B_z and B_r in Figures 3 and 4 by extrapolating the observed trends to the estimated magnetic equator location. For the magnetic field strength 3 nT and curvature radius of $0.4 R_E$ at the equator, the κ parameter [Büchner and Zelenyi, 1987; Zelenyi *et al.*, 1990] becomes unity with proton energy of $\sim 3 \text{ keV}$, meaning that some fraction of protons can be nonadiabatic owing to local this small spatial scale, though further study is needed to assess these aspects.

3.4.5. The Plasma Behavior During Incompressible Thinning and Formation of the Weak Field Region in the Near-Earth Tail

[40] During cross-tail current sheet thinning, there were no temporal variations for total pressure and density: $\delta P_t \sim 0$ and $\delta n \sim 0$ at various locations in the current sheet. Our observation is consistent with the result from Cluster observation studied by Petrukovich *et al.* [2007] in the sense that the plasma density was not associated with the increased current density. There was a particular layer or flux tube that showed the increased magnetic pressure and the decreased plasma pressure: $\delta P_b > 0$ and $\delta P < 0$ or $\delta T < 0$ with $\delta n \sim 0$ and $\delta P_t \sim 0$. The constant total pressure is consistent with a quasi-static current sheet. The magnetic and plasma pressure changes are in accord with keeping total pressure constant. In this way, the plasma sheet can evolve without changing the rest of the magnetotail, but can evolve only within a radially limited region of the plasma sheet. The temperature changes during the thinning can be understood as an incompressible process. Because the density is found to be weakly variable of the latitudinal location, the temporally constant behavior observed for all location indicates the densities in the flux tubes also stayed constant during the thinning process. Hence using the multispacecraft observation, it is possible to diagnose that the changes of the plasma state in the flux tube was incompressible. For loss-less flux tubes, nV will be constant where V is the flux tube

volume per unit flux. In the process of the cross-tail current sheet thinning, it follows that $\delta n \sim 0$ indicates $\delta V \sim 0$. The flux tubes changed their structure during thinning as observed by curvature changes, but their volume will not change dramatically. This constant volume may explain the formation of the weak magnetic field region in the near-Earth tail. Since the latitudinal dimension will be thinner, its width at the equator may expand to make the equatorial magnetic field strength weaker. At present we are not able to suggest any mechanism for the thinning behavior ($\delta P_b > 0$), but at least we show that this process is possible without having compression of the plasma sheet.

4. Conclusion

[41] Understanding the behavior of the plasma sheet in the magnetotail is essential for understanding energy transfer within the magnetosphere, its stability and instability problems and magnetosphere-ionosphere relationships. Five spacecraft THEMIS measurements during a small substorm on April 8, 2008 are used to examine the current sheet and its thinning processes in the near-Earth tail in terms of structure and MHD force balance. These measurements, all near $X = -11$ and $Y = 4 R_E$, were used to derive the latitudinal profile of plasma and magnetic pressures and magnetic field line curvatures within $1.5 R_E$ of the equator.

[42] 1. Plasma sheet magnetic pressure increased during thinning while temperature decreased and density remained nearly constant leading to a total pressure that remained essentially constant both before and during thinning. Such thinning with constant pressure is in conflict with the conventional picture where adding magnetic flux to the tail lobe leads to the enhanced tail compression, higher pressure and current sheet thinning.

[43] 2. There was a significant latitudinal gradient in the total pressure in the outer part of the current sheet at a distance $1 R_E$ from the magnetic equator both before and during the thinning, while the total pressure of the inner part showed the latitudinal gradient only during the thinning.

[44] 3. The latitudinal component of the magnetic field line curvature had a positive sign and remained constant in the outer part of the current sheet both before and during thinning. The inner part, however, had a zero or negative sign before the thinning that changed to positive during the thinning. This change of the geometry indicates the earthward motion of the cross tail current.

[45] 4. The thinning is a MHD force-balanced self-evolving process.

[46] 5. The thinning is a change of flux tube structure in length and curvature, but not largely in volume.

[47] 6. The thinning changes the radial profile of plasma pressure, and is associated with the increase in current density locally in the near-Earth tail.

[48] In conclusion, our event demonstrates that the cross-tail current sheet thinning is not necessarily and not primarily caused by an increase in lobe field strength as generally envisioned in the conventional picture of tail evolution during the growth phase of substorms. The cross-tail current sheet thinning before the substorm onset occurs in the near-equatorial region of the plasma sheet and can evolve internally. The observed plasma sheet behavior, spatial changes, and formation of the intense current density in the near-

Earth tail can be comprehensively understood as the behavior of a quasi-static incompressible plasma sheet. It should be emphasized that the presence of the incompressible thinning before substorm onset provides an explanation for the formation of the near-Earth neutral line and the development of the high β regions as a result of the thinning.

Appendix A: Plasma Moment Data

[49] The moment data for ions and electrons used in this study are calculated from the distribution function measured by ESA and SST instruments. A pair of ESA instruments obtained the three-dimensional distribution function over the energy range 6 eV/q to 25 keV/q for ions and from 7 eV to 30 keV for electrons for every 3 s spin period. SST instruments detect 25 keV to 6 MeV for protons and 25 keV to ~ 900 keV for electrons. Four detectors cover out of spin plane and the three-dimensional distribution is obtained for every spin having the spin-plane angular resolution of ~ 20 degree.

[50] Figure A1 shows ion and electron energy-time spectrum from ESA and SST instruments for THEMIS P4, which was located the closest to the magnetic equator throughout the substorm. Since the THEMIS plasma data analysis takes into account the measured spacecraft potential by Langmuir sensors [McFadden *et al.*, 2008b; Bonnell *et al.*, 2008], photoelectrons are effectively removed in the electron moment calculations. Figure A2 demonstrates SST measurements and their contribution to the calculated moment values. The top two panels are spin-plane angular spectrums that are derived by integrating energy fluxes over energies and over all four detectors at fields of view of ~ 30 degree at $+55, +25, -25, -55$ degree out of spin plane. Sun pulse contaminations on SST is seen in the direction of ± 180 degree in x-y plane in the Despan Sun Oriented L-oriented or DSL coordinate system and are removed in calculating moments by masking all contaminated channels in the relevant direction. Bottom two panels show comparison of the calculated moment values with (magenta) and without (black) SST data. It turned out that before the dipolarization onset at ~ 7 UT, the contribution of the SST to the moment values is small for all five probes, though we use both instruments to compute moments for analysis.

[51] In the calculation of the pressure and temperature, it was assumed that the plasma distribution is isotropic. The temperatures from ESA and SST data are given by $T_{ESA} = (T_{xx} + T_{yy} + T_{zz})/3$ and $T_{SST} = (T_{xx} + T_{yy})/2$ respectively in the Despan Sun Oriented L-oriented coordinate system. Owing to the coarse resolution in the z direction of SST, moments are calculated separately for the distribution function f_{ESA} for the energy range covered by ESA and f_{SST} for energy range covered by SST, where $f = f_{ESA} + f_{SST}$ is the unified distribution function. The zeroth-, first- and second- order of the moments are by definition

$$n = \int f d^3 \mathbf{u} \quad (A1)$$

$$n\mathbf{U} = \int \mathbf{u} f d^3 \mathbf{u} \quad (A2)$$

$$P_{\alpha\alpha} = m \int (u_{\alpha} - U_{\alpha})^2 f d^3 \mathbf{u} = m \int u_{\alpha}^2 f d^3 \mathbf{u} - mnU_{\alpha}^2 \quad (A3)$$

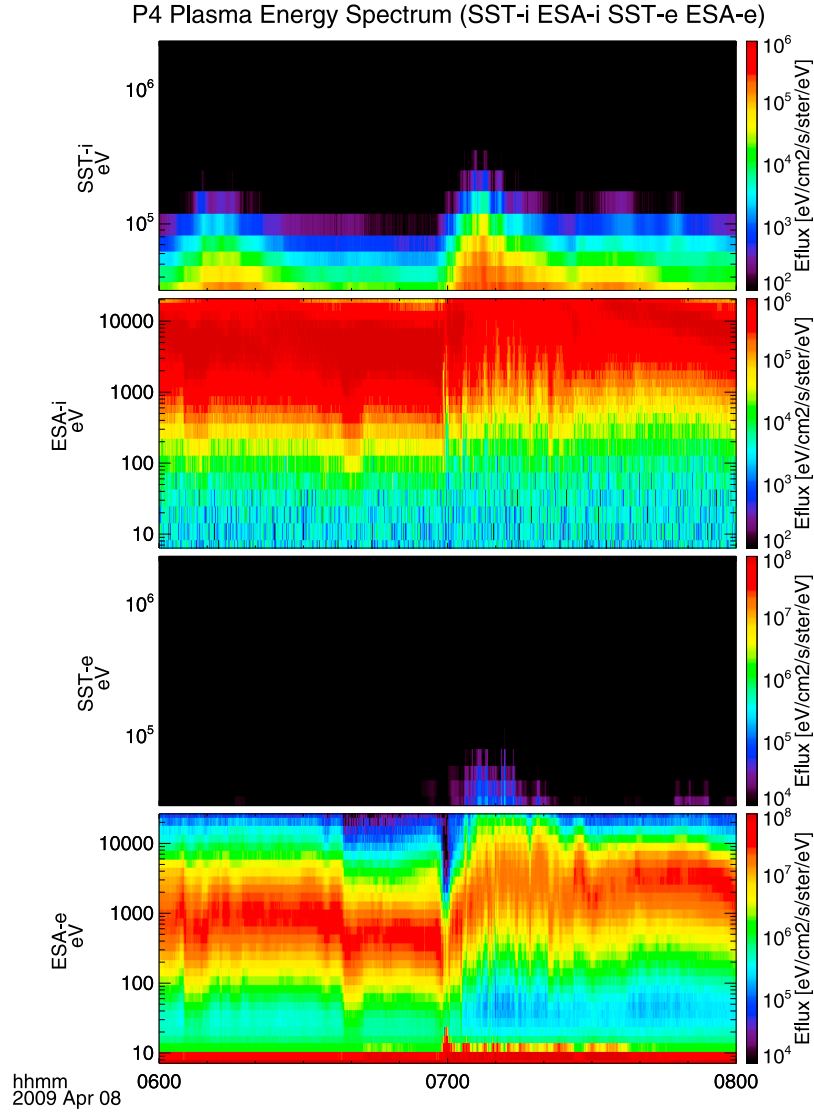


Figure A1. Energy-time diagrams for ion and electron obtained by THEMIS P4 that was located at the closest to the magnetic equator. Each energy-time diagram consists of SST and ESA measurements.

where n is number density, \mathbf{U} the average velocity vector, $P_{\alpha\alpha}$ the diagonal component of pressure tensor, and m is mass of the species. The diagonal component of the temperature tensor T_{α} is $T_{\alpha\alpha} = P_{\alpha\alpha}/nk$, where k is the Boltzman constant. We have

$$n = \int f_{ESA} + f_{SST} d^3 \mathbf{u} = n_{ESA} + n_{SST} \quad (\text{A4})$$

$$n\mathbf{U} = \int \mathbf{u}(f_{ESA} + f_{SST}) d^3 \mathbf{u} = n_{ESA}\mathbf{U}_{ESA} + n_{SST}\mathbf{U}_{SST} \quad (\text{A5})$$

$$\begin{aligned} P_{\alpha\alpha} &= m \int u_{\alpha}^2 (f_{ESA} + f_{SST}) d^3 \mathbf{u} - mnU_{\alpha}^2 \\ &= P_{\alpha\alpha,ESA} + mn_{ESA}U_{\alpha,ESA}^2 + P_{\alpha\alpha,SST} + mn_{SST}U_{\alpha,SST}^2 - mnU_{\alpha}^2 \end{aligned} \quad (\text{A6})$$

For the moment calculation, the distribution functions are averaged for 3 s and 300 s for ESA and SST respectively.

[52] The validity of the isotropy assumption is checked as follows. We use the ratios between the components of pressure tensor using the ion ESA distribution function. The degree of the deviation from the isotropic distributions $P_{\alpha\alpha}/P_{\beta\beta} - 1$ and $P_{\alpha\beta}/P_{\alpha\alpha}$ are examined for the interval of the interest and found to vary within 5% for the most of the interval for all probes. Particularly from 0600 UT to 0656 UT, the means of these values are 0 to 2% with standard deviation of 2 to 7%. However, the exception exists in P2 observation from 0630 UT to 0645 UT. Within this 15 min interval, $P_{\alpha\alpha}/P_{\beta\beta} - 1$ was -20% on the average with the standard deviation of $\sim 10\%$ in the Despan Sun Oriented L-oriented coordinate system. Apart from this observation by P2, the assumption of the isotropic distribution is valid with the accuracy of $\sim 5\%$ for 3 s resolution data.

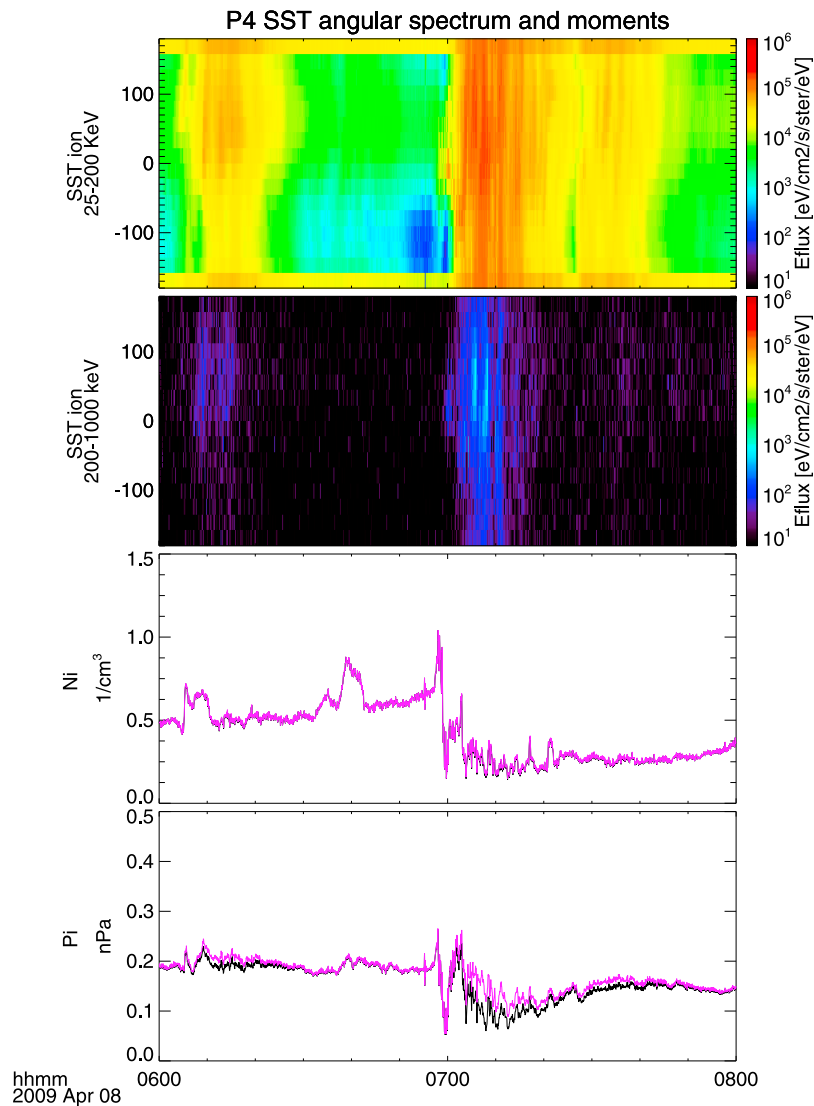


Figure A2. SST angular spectrums and moments calculated with and without SST.

[53] **Acknowledgments.** MS thanks L. Chen and C. Z. Cheng for helpful comments and insights. MS is also grateful for D. Wolf and J. Yang for important aspects and information obtained by the equilibrium version of the Rice Convection Model. We thank one of reviewers for pointing out a validity of the MHD regime. We acknowledge S. Mende, C. T. Russell, and I. Mann for THEMIS GBO/GMAGs, and the CSA for support of the CARISMA network. Solar wind data are from NASA OMNIWeb Plus Interface. This research was supported in part by an appointment to the NASA Postdoctoral Program at Goddard Space Flight Center, administered by Oak Ridge Associated Universities through a contract with NASA. This research is supported in part by the National Science Council of the Republic of China under grant NSC 97-2111-M-008-006-MY3 to National Central University.

[54] Masaki Fujimoto thanks the reviewers for their assistance in evaluating this paper.

References

- Angelopoulos, V. (2008), The THEMIS Mission, *Space Sci. Rev.*, *141*, 5–34, doi:10.1007/s11214-008-9336-1.
- Auster, H. U., et al. (2008), The THEMIS fluxgate magnetometer, *Space Sci. Rev.*, *141*, 235–264, doi:10.1007/s11214-008-9365-9.
- Bhattacharjee, A., Z. W. Ma, and X. Wang (1998), Ballooning instability of a thin current sheet in the high-Lundquist-number magnetotail, *Geophys. Res. Lett.*, *25*, 861–864.
- Bonnell, J. W., F. S. Mozer, G. T. Delory, A. J. Hull, R. E. Ergun, C. M. Cully, V. Angelopoulos, and P. R. Harvey (2008), The electric field instrument (EFI) for THEMIS, *Space Sci. Rev.*, *141*, 303–341, doi:10.1007/s11214-008-9469-2.
- Büchner, J., and L. M. Zelenyi (1987), Chaotization of the electron motion as the cause of an internal magnetotail instability and the substorm onset, *J. Geophys. Res.*, *92*, 13,456–13,466.
- Cheng, C. Z., and A. T. Y. Lui (1998), Kinetic ballooning instability for substorm onset and current disruption observed by AMPTE/CCE, *Geophys. Res. Lett.*, *25*, 4091–4094.
- Erickson, G. M., and R. A. Wolf (1980), Is steady convection possible in the Earth's magnetotail?, *Geophys. Res. Lett.*, *7*, 897–900.
- Fairfield, D., and N. Ness (1970), Configuration of the geomagnetic tail during substorms, *J. Geophys. Res.*, *75*, 7032–7047.
- Frey, S., V. Angelopoulos, M. Bester, J. Bonnell, T. Phan, and D. Rummel (2008), Orbit design for the THEMIS mission, *Space Sci. Rev.*, *141*, 61–89, doi:10.1007/s11214-008-9441-1.
- Hau, L.-N. (1991), Effects of steady state adiabatic convection on the configuration of the near-Earth plasma sheet, 2, *J. Geophys. Res.*, *96*, 5591–5596.
- Hau, L.-N., R. A. Wolf, G.-H. Voigt, and C. C. Wu (1989), Steady state magnetic field configurations for the Earth's magnetotail, *J. Geophys. Res.*, *94*, 1303–1316.
- Horton, W., H. Wong, J. Van Dam, and C. Crabtree (2001), Stability properties of high pressure geotail flux tubes, *J. Geophys. Res.*, *106*, 18,803–18,822.
- Hurricane, O. (1997), MHD ballooning stability of a sheared plasma sheet, *J. Geophys. Res.*, *102*, 19,903–19,911.

- Hurricane, O., R. Pellat, and F. Coroniti (1995), A new approach to low-frequency “MHD-like” waves in magnetospheric plasmas, *J. Geophys. Res.*, *100*, 19,421–19,428.
- Kaufmann, R. L. (1987), Substorm currents: Growth phase and onset, *J. Geophys. Res.*, *92*, 7471–7486.
- Kaufmann, R. L., D. J. Larson, I. D. Kontodinas, and B. M. Ball (1997), Force balance and substorm effects in the magnetotail, *J. Geophys. Res.*, *102*, 22,141–22,154.
- Le Contel, O., R. Pellat, and A. Roux (2000a), Self-consistent quasi-static parallel electric field associated with substorm growth phase, *J. Geophys. Res.*, *105*, 12,945–12,954.
- Le Contel, O., R. Pellat, and A. Roux (2000b), Self-consistent quasi-static radial transport during the substorm growth phase, *J. Geophys. Res.*, *105*, 12,929–12,944.
- Lee, D. Y., and R. Wolf (1992), Is the Earth’s magnetotail balloon unstable?, *J. Geophys. Res.*, *97*, 19,251–19,257.
- Liu, W. W., E. F. Donovan, J. Liang, I. Voronkov, E. Spanswick, P. T. Jayachandran, B. Jackel, and M. Meurant (2007), On the equatorward motion and fading of proton aurora during substorm growth phase, *J. Geophys. Res.*, *112*, A10217, doi:10.1029/2007JA012495.
- Lui, A. T. Y., R. E. Lopez, B. J. Anderson, K. Takahashi, L. J. Zanetti, R. W. McEntire, T. A. Potemra, D. M. Klumpar, E. M. Greene, and R. Strangeway (1992), Current disruptions in the near-Earth neutral sheet region, *J. Geophys. Res.*, *97*, 1461–1480.
- Maezawa, K. (1975), Magnetotail boundary motion associated with geomagnetic substorms, *J. Geophys. Res.*, *80*, 3543–3550.
- McFadden, J. P., C. W. Carlson, D. Larson, M. Ludlam, R. Abiad, B. Elliott, P. Turin, M. Marckwordt, and V. Angelopoulos (2008a), The THEMIS ESA plasma instrument and in-flight calibration, *Space Sci. Rev.*, *141*, 277–302, doi:10.1007/s11214-008-94402.
- McFadden, J. P., C. W. Carlson, D. Larson, J. Bonnell, F. Mozer, V. Angelopoulos, K.-H. Glassmeier, and U. Auster (2008b), THEMIS ESA first science results and performance issues, *Space Sci. Rev.*, *141*, 407–508, doi:10.1007/s11214-008-94331.
- Miura, A. (2004), Validity of the fluid description of critical β and Alfvén time scale of ballooning instability onset in the near-Earth collisionless high- β plasma, *J. Geophys. Res.*, *109*, A02211, doi:10.1029/2003JA009924.
- Miura, A., S. Ohtani, and T. Tamao (1989), Ballooning instability and structure of diamagnetic hydromagnetic waves in a model magnetosphere, *J. Geophys. Res.*, *94*, 15,231–15,242.
- Nagai, T., T. Mukai, T. Yamamoto, A. Nishida, S. Kokubun, and R. P. Lepping (1997), Plasma sheet pressure changes during the substorm growth phase, *Geophys. Res. Lett.*, *24*, 963–966.
- Nishida, A., and E. W. Hones Jr. (1974), Association of plasma sheet thinning with neutral line formation in the magnetotail, *J. Geophys. Res.*, *79*, 535–547.
- Pellat, R., O. Le Contel, A. Roux, S. Perraut, O. Hurricane, and F. V. Coroniti (2000), Self-consistent kinetic approach for low frequency and quasi-static electromagnetic perturbations in magnetic-mirror confined plasmas, in *Transport and Energy Conversion in the Heliosphere*, *Lect. Notes Phys.*, vol. 553, edited by J.-P. Roselot, L. Klein, and J.-C. Vial, pp. 165–214, Springer, New York.
- Petrukovich, A. A., W. Baumjohann, R. Nakamura, A. Runov, A. Balogh, and H. Rème (2007), Thinning and stretching of the plasma sheet, *J. Geophys. Res.*, *112*, A10213, doi:10.1029/2007JA012349.
- Pritchett, P. L., and F. V. Coroniti (2010), A kinetic ballooning/interchange instability in the magnetotail, *J. Geophys. Res.*, *115*, A06301, doi:10.1029/2009JA014752.
- Pu, Z., A. Korth, Z. Chen, R. Friedel, Q. Zong, X. Wang, M. Hong, S. Fu, Z. Liu, and T. Pulkkinen (1997), MHD drift ballooning instability near the inner edge of the near-Earth plasma sheet and its application to substorm onset, *J. Geophys. Res.*, *102*, 14,397–14,406.
- Raeder, J., P. Zhu, Y. Ge, and G. Siscoe (2010), Open Geospace General Circulation Model simulation of a substorm: Axial tail instability and ballooning mode preceding substorm onset, *J. Geophys. Res.*, *115*, A00116, doi:10.1029/2010JA015876.
- Saito, M. H., Y. Miyashita, M. Fujimoto, I. Shinohara, Y. Saito, K. Liou, and T. Mukai (2008), Ballooning mode waves prior to substorm-associated dipolarizations: Geotail observations, *Geophys. Res. Lett.*, *35*, L07103, doi:10.1029/2008GL033269.
- Saito, M. H., L.-N. Hau, C.-C. Hung, Y.-T. Lai, and Y.-C. Chou (2010), Spatial profile of magnetic field in the near-Earth plasma sheet prior to dipolarization by THEMIS: Feature of minimum B, *Geophys. Res. Lett.*, *37*, L08106, doi:10.1029/2010GL042813.
- Samson, J. C., and P. Dobias (2005), Explosive instabilities and substorm intensifications in the Earth’s magnetotail, in *Multiscale Coupling of Sun-Earth Processes*, edited by A. T. Y. Lui, Y. Kamide, and G. Consolini, pp. 235–251, Elsevier, New York.
- Shibasaki, K. (2003), Signature of energy release and particle acceleration observed by the Nobeyama radioheliograph, in *Lect. Notes Phys.*, vol. 612, edited by K.-L. Klein, pp. 96–108, Springer, New York.
- Sitnov, M. I., and K. Schindler (2010), Tearing stability of a multiscale magnetotail current sheet, *Geophys. Res. Lett.*, *37*, L08102, doi:10.1029/2010GL042961.
- Wang, C.-P., L. R. Lyons, T. Nagai, and J.C. Samson (2004), Midnight radial profiles of the quiet and growth-phase plasma sheet: The Geotail observations, *J. Geophys. Res.*, *109*, A12201, doi:10.1029/2004JA010590.
- Wanliss, J. A., J. C. Samson, and E. Friedrich (2000), On the use of photometer data to map dynamics of the magnetotail current sheet during substorm growth phase, *J. Geophys. Res.*, *105*, 673–684.
- Vasyliunas, V. M. (1970), Mathematical models of magnetospheric convection and its coupling to the ionosphere, in *Particles and Fields in the Magnetosphere*, edited by B. M. McCormac, pp. 60–71, Reidel, Dordrecht, Netherlands.
- Zaharia, S., and C. Z. Cheng (2003), Near-Earth thin current sheets and Birkeland currents during substorm growth phase, *Geophys. Res. Lett.*, *30*(17), 1883, doi:10.1029/2003GL017456.
- Zelenyi, L., A. Galeev, and C. F. Kennel (1990), Ion precipitation from the inner plasma sheet due to stochastic diffusion, *J. Geophys. Res.*, *95*, 3871–3882.
- Zhu, P., C. R. Sovinec, C. C. Hegna, A. Bhattacharjee, and K. Germaschewski (2007), Nonlinear ballooning instability in the near-Earth magnetotail: Growth, structure, and possible role in substorms, *J. Geophys. Res.*, *112*, A06222, doi:10.1029/2006JA011991.

V. Angelopoulos, Institute of Geophysics and Planetary Physics, University of California, Los Angeles, CA 90095, USA.

U. Auster, Institut für Geophysik und Extraterrestrische Physik der Technischen Universität Braunschweig, Mendelssohnstr. 3, D-38106 Braunschweig, Germany.

J. W. Bonnell, D. Larson, and J. P. McFadden, Space Science Laboratory, University of California, Berkeley, CA 94720, USA.

D. Fairfield, G. Le, and M. H. Saito, NASA Goddard Space Flight Center, Greenbelt, MD 20771, USA. (miho.hasegawa@nasa.gov)

L.-N. Hau, Institute of Space Science, National Central University, Zhongli, 32001, Taiwan.